

# Simulations of energetic particle driven instabilities in CFQS

journal or publication title	Nuclear Fusion
volume	62
number	10
page range	106010
year	2022-08-30
NAIS	13373
URL	<a href="http://hdl.handle.net/10655/00013469">http://hdl.handle.net/10655/00013469</a>

doi: <https://doi.org/10.1088/1741-4326/ac843a>



ACCEPTED MANUSCRIPT

## Simulations of energetic particle driven instabilities in CFQS

To cite this article before publication: Hao Wang *et al* 2022 *Nucl. Fusion* in press <https://doi.org/10.1088/1741-4326/ac843a>

### Manuscript version: Accepted Manuscript

Accepted Manuscript is “the version of the article accepted for publication including all changes made as a result of the peer review process, and which may also include the addition to the article by IOP Publishing of a header, an article ID, a cover sheet and/or an ‘Accepted Manuscript’ watermark, but excluding any other editing, typesetting or other changes made by IOP Publishing and/or its licensors”

This Accepted Manuscript is © 2022 IAEA, Vienna.

During the embargo period (the 12 month period from the publication of the Version of Record of this article), the Accepted Manuscript is fully protected by copyright and cannot be reused or reposted elsewhere. As the Version of Record of this article is going to be / has been published on a subscription basis, this Accepted Manuscript is available for reuse under a CC BY-NC-ND 3.0 licence after the 12 month embargo period.

After the embargo period, everyone is permitted to use copy and redistribute this article for non-commercial purposes only, provided that they adhere to all the terms of the licence <https://creativecommons.org/licenses/by-nc-nd/3.0>

Although reasonable endeavours have been taken to obtain all necessary permissions from third parties to include their copyrighted content within this article, their full citation and copyright line may not be present in this Accepted Manuscript version. Before using any content from this article, please refer to the Version of Record on IOPscience once published for full citation and copyright details, as permissions will likely be required. All third party content is fully copyright protected, unless specifically stated otherwise in the figure caption in the Version of Record.

View the [article online](#) for updates and enhancements.

# Simulations of energetic particle driven instabilities in CFQS

Hao WANG (王灏)<sup>1</sup>, Yasushi TODO (藤堂 泰)<sup>1</sup>, Jie HUANG (黄杰)<sup>2,3</sup>, Yasuhiro SUZUKI (鈴木 康浩)<sup>4</sup>, Akihiro SHIMIZU (清水 昭博)<sup>1</sup>, Kunihiro OGAWA (小川 国大)<sup>1</sup>, Xianqu WANG (王 先驱)<sup>5</sup>, Panith ADULSIRISWAD<sup>1</sup>

<sup>1</sup>National Institute for Fusion Science, National Institutes of Natural Sciences, Toki, Japan

<sup>2</sup>Forschungszentrum Jülich GmbH, Jülich, Germany

<sup>3</sup>Huazhong University of Science and Technology, Wuhan, China

<sup>4</sup>Hiroshima University, Higashihiroshima, Japan

<sup>5</sup>Southwest Jiaotong University, Chengdu, China

E-mail: wanghao@nifs.ac.jp

July 25, 2022

**Abstract.** A nonlinear simulation of the energetic particle driven instabilities in the Chinese First Quasi-Axisymmetric Stellarator (CFQS) has been conducted for the first time. MEGA, a hybrid simulation code for energetic particles interacting with a magneto-hydrodynamic (MHD) fluid, was used in the present work. Both the  $m/n = 3/1$  energetic-particle-mode (EPM) like mode and the  $m/n = 5/2$  toroidal Alfvén eigenmode (TAE) were found, where  $m$  is the poloidal mode number and  $n$  is the toroidal mode number. Four important results were obtained as follows. First, the instability in the CFQS in three-dimensional form was shown for the first time. Second, strong toroidal mode coupling was found for the spatial profiles, and it is consistent with the theoretical prediction. Third, the resonant condition caused by the absence of axial symmetry in CFQS was demonstrated for the first time. The general resonant condition is  $f_{mode} = Nf_{\phi} - Lf_{\theta}$ , where  $f_{mode}$ ,  $f_{\phi}$ , and  $f_{\theta}$  are mode frequency, particle toroidal transit frequency, and particle poloidal transit frequency, respectively;  $N$  and  $L$  are arbitrary integers, represent toroidal and poloidal resonance numbers. For EPM-like mode, the dominant and subdominant resonant conditions are  $f_{mode} = 3f_{\phi} - 7f_{\theta}$  and  $f_{mode} = f_{\phi} - f_{\theta}$ , respectively. For TAE, the dominant and subdominant resonant conditions are  $f_{mode} = 4f_{\phi} - 9f_{\theta}$  and  $f_{mode} = 2f_{\phi} - 3f_{\theta}$ , respectively. On the one hand, the toroidal resonance numbers are different from the toroidal mode numbers by 2. This indicates that the 2-fold rotational symmetry affects the resonance condition. On the other hand, the subdominant resonances satisfy  $N = n$ , which is expected for the axisymmetric plasmas and most of the toroidal plasmas including stellarators. Fourth, the nonlinear frequency chirpings in CFQS were demonstrated for the first time. Hole and clump structures were formed in the pitch angle and energy phase space, and the particles comprising the hole and clump were kept resonant with the modes during the mode frequencies chirping.

1  
2  
3 *Simulations of EP driven instabilities in CFQS: H. Wang, Y. Todo, J. Huang et al* 2

## 4 **1. Introduction**

5  
6  
7 Nuclear fusion may solve the energy crisis of human beings. For magnetic confinement  
8 fusion, the most important two kinds of devices are the tokamak and stellarator. The  
9 tokamak is good for reducing neoclassical transport, and the stellarator for steady state  
10 operation. The QA device is a kind of tokamak-like stellarator, or a combination of  
11 tokamak and stellarator. On the one hand, as a stellarator it does not require inductive  
12 plasma current, and thus it is very appropriate for steady state operation; on the other  
13 hand, because of its special quasi-symmetric configuration, it weakens the neoclassical  
14 transport, and thus the confinement level is better than a conventional stellarator[1].  
15 Because of these advantages, two QA devices, the CHS-qa[2] and NCSX[3], were  
16 designed many years ago in Japan and the USA, respectively. Also, the QuASDEX  
17 is being designed in Germany. Now a QA device named the Chinese First Quasi-  
18 Axisymmetric Stellarator (CFQS) is being constructed by National Institute for Fusion  
19 Science (Japan) and Southwest Jiaotong University (China) under a framework of  
20 international collaboration. The first plasma will be generated soon[4, 5]. After that  
21 auxiliary heating, including both electron cyclotron resonance heating (ECRH) and NBI,  
22 will be applied. Many studies based on the CFQS have already been carried out and  
23 they cover different topics like configuration optimization, MHD instabilities, energetic  
24 particle driven instabilities, etc.[6–8]

25  
26  
27 Energetic particle driven instability is an important issue for fusion research. During  
28 energetic particle driven instabilities, the radial transport of energetic particles will  
29 be enhanced and a lot of energetic particles lost, and thus heating performance will  
30 deteriorate, and the confinement level will decrease. The Alfvén eigenmode (AE) is  
31 a typical dangerous energetic particle driven instability. During AE activities more  
32 than half of energetic particles can be lost[9]. Thus it is important to investigate the  
33 AE properties in the CFQS before its first plasma, in order to avoid a dangerous  
34 configuration or operation. Similarly, the energetic-particle-mode (EPM) is also  
35 dangerous for its large amplitude and strong transport effect[10–12].

36  
37  
38 The AE behaviors in the CFQS have already been investigated in Ref. [8]. The  
39 linear properties of many different AEs including  $m/n = 3/1$  mode and  $m/n = 5/2$   
40 mode were analyzed under various conditions like the rotational transform  $\iota$  profiles and  
41 plasma pressure profiles. As the first literature of AE properties in the CFQS, Ref. [8]  
42 covers many issues of interest, but there are still a lot of gaps left, for example nonlinear  
43 mode properties, resonant conditions, 3-dimensional visualization, and energetic particle  
44 transport. The present paper will fill in the above gaps and it is organized as follows. In  
45 section 2 the simulation model and conditions are described. In section 3 the simulation  
46 results of an EPM-like mode are presented. In section 4 the simulation results of the  
47 toroidal Alfvén eigenmode (TAE) are presented. In section 5 the main conclusions are  
48 summarized.

49  
50  
51  
52  
53  
54  
55  
56  
57  
58  
59  
60

## 2. Simulation model and parameters

A hybrid simulation code, MEGA[13–15], for energetic particles interacting with a magnetohydrodynamic (MHD) fluid is used for the simulations of the energetic particle driven instabilities in the CFQS. The hybrid model is widely used in the fusion community[16]. There are two versions of MEGA. In the conventional version, only the energetic particles are described by the kinetic equations, while in the extended version both the energetic particles and the thermal ions are described kinetically. In the present work, the conventional version is applied. The MHD equations with the energetic-ion effects are given by

$$\frac{\partial \rho}{\partial t} = -\nabla \cdot (\rho \mathbf{v}) + \nu_n \Delta (\rho - \rho_{eq}), \quad (1)$$

$$\begin{aligned} \rho \frac{\partial}{\partial t} \mathbf{v} = & -\rho \boldsymbol{\omega} \times \mathbf{v} - \rho \nabla \left( \frac{v^2}{2} \right) - \nabla p + (\mathbf{j} - \mathbf{j}'_h) \\ & \times \mathbf{B} - \nabla \times (\nu \rho \boldsymbol{\omega}) + \frac{4}{3} \nabla (\nu \rho \nabla \cdot \mathbf{v}), \end{aligned} \quad (2)$$

$$\frac{\partial \mathbf{B}}{\partial t} = -\nabla \times \mathbf{E}, \quad (3)$$

$$\begin{aligned} \frac{\partial p}{\partial t} = & -\nabla \cdot (p \mathbf{v}) - (\gamma - 1) p \nabla \cdot \mathbf{v} \\ & + (\gamma - 1) \left[ \nu \rho \omega^2 + \frac{4}{3} \nu \rho (\nabla \cdot \mathbf{v})^2 + \eta \mathbf{j} \cdot (\mathbf{j} - \mathbf{j}_{eq}) \right] \\ & + \nu_n \Delta (p - p_{eq}), \end{aligned} \quad (4)$$

$$\mathbf{E} = -\mathbf{v} \times \mathbf{B} + \eta (\mathbf{j} - \mathbf{j}_{eq}), \quad (5)$$

$$\boldsymbol{\omega} = \nabla \times \mathbf{v}, \quad (6)$$

$$\mathbf{j} = \frac{1}{\mu_0} \nabla \times \mathbf{B}, \quad (7)$$

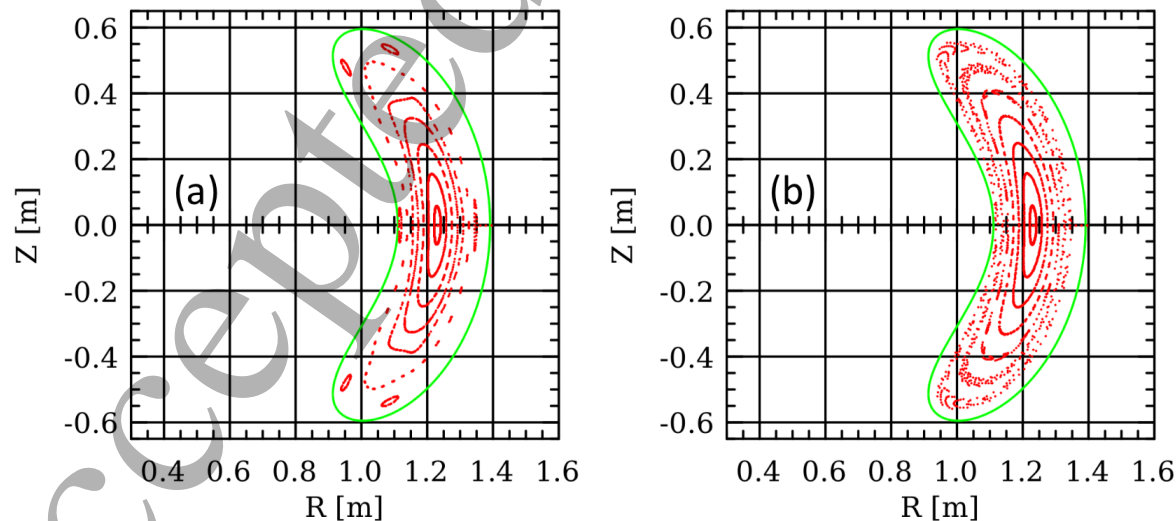
where  $\mu_0$  is the vacuum magnetic permeability,  $\gamma$  is the adiabatic constant,  $\nu$  and  $\nu_n$  are artificial viscosity and diffusion coefficients, chosen to maintain numerical stability, and all the other quantities are conventional. The subscript  $h$  denotes hot particles, and in the present work, the hot particles represent energetic ones. We avoid using the subscript  $EP$  to keep consistent with previous literature. The subscript ‘ $eq$ ’ represents equilibrium variables. The MHD equations are solved using a fourth order (in both space and time) finite difference scheme.

The energetic particles are described by the drift-kinetic equations. The modules of gyrokinetic approach is included in MEGA, but the gyrokinetic module is turned off in the simulations presented in this paper, because of three reasons: (1) the Larmor radius of energetic particle  $\rho_{EP}$  in CFQS is very small and the product of the perpendicular wave number and  $\rho_{EP}$  is much less than the unity; (2) normally the mode linear properties like frequency and mode structure are only weakly influenced by finite Larmor radius effect[17, 18]; and (3) drift-kinetic approach is more efficient for computing

1  
2  
3 *Simulations of EP driven instabilities in CFQS: H. Wang, Y. Todo, J. Huang et al.* 4

5 resources. The  $\delta f$  particle-in-cell (PIC) method is applied, and the equations of motion  
6 for each marker particle are solved using a fourth order Runge-Kutta method. For more  
7 details of the equations of MEGA, Ref. [13–15, 19] may be good references.

8  
9 Both the VMEC and HINT codes are popular ones for plasma equilibrium[20, 21].  
10 Although the HINT equilibrium data needs to be calculated based on the existing VMEC  
11 equilibrium data, and HINT takes much more computational resources than VMEC,  
12 HINT still has two obvious advantages for MEGA simulation. First, HINT can model  
13 complex magnetic field structures such as magnetic islands, which means that the results  
14 of HINT are closer to the real situation. Second, HINT uses  $(R, \phi, z)$  coordinates, which  
15 are the same as MEGA, thus the equilibrium data generated by HINT can be used in  
16 MEGA more conveniently without coordinate conversion. Because of the above two  
17 advantages, in the present paper, HINT equilibria data are used for the simulation. The  
18 existing VMEC equilibrium data describes a representative case in the CFQS. Based  
19 on the existing VMEC equilibrium data, by adjusting the plasma current to 5 kA and  
20 20 kA, finally, two different HINT equilibria data are generated. The MEGA simulation  
21 in the present paper is implemented based on these two equilibria data. They correspond  
22 to the case with magnetic islands and that without a magnetic island, as shown in Fig.1.  
23 The HINT equilibrium is not the same as the VMEC equilibrium, which can be seen from  
24 Fig. 2. For the case with magnetic islands, the pressure profile is significantly flattened  
25 near the plasma edge, which corresponds to those six magnetic islands in Fig. 1(a). In  
26 addition, the  $\iota$  profile is also slightly different in these cases, as shown in Fig. 3. For the  
27 case with magnetic islands, the  $\iota$  profile intersects  $\iota = 1/3$  line near the plasma edge,  
28 which corresponds to those six magnetic islands in Fig. 1(a).  
29  
30  
31  
32  
33  
34  
35



54  
55 **Figure 1.** Poloidal cross sections with Poincaré plots of the magnetic configurations  
56 of two cases (a) with magnetic islands and (b) without magnetic island. Both figures  
57 are plotted at  $\phi=0$ .  
58

59 The following four parameters for the simulation are based on the CFQS design[4, 5]:  
60

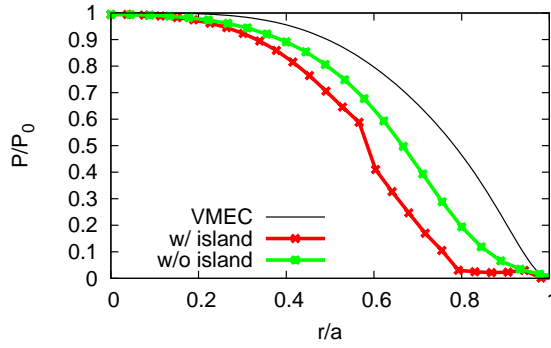


**Figure 2.** The normalized pressure profiles of VMEC, HINT with magnetic islands, and HINT without magnetic island.  $P_0$  represents the pressure on the magnetic axis.

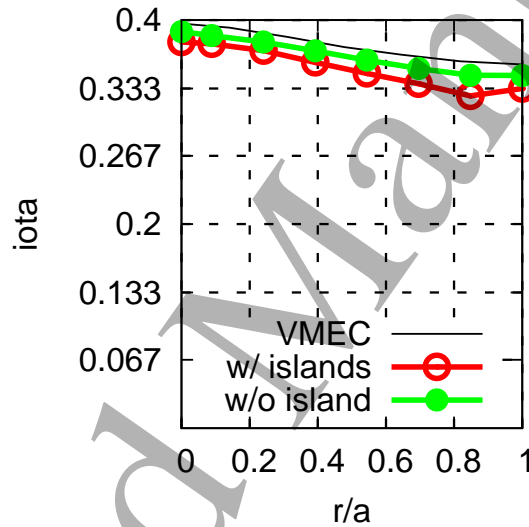


**Figure 3.** Rotational transform  $\iota$  profiles of VMEC, HINT with magnetic islands, and HINT without magnetic island.

1) The plasma major radius  $R_0 = 1.0$  m on average. 2) The magnetic field strength on the magnetic axis  $B_0 = 1.0$  T on average. 3) The electron density in plasma center  $n_e = 1.0 \times 10^{19} \text{ m}^{-3}$ . 4) The electron temperature in plasma center  $T_e = 2.1$  keV. And finally, 5) the  $\beta$  value of plasma in the core region is 1.0%. Hydrogen plasma is assumed, which is the same as the CFQS design. The number of field period  $N_{fp}=2$ , is the same as the CFQS design and equilibrium calculation. The neutral beam injection (NBI) system of the CFQS is transferred from the CHS device where the NBI energy  $E_{NBI} = 40$  keV, and thus this parameter is used for the present work. A slowing-down energetic particle distribution function is assumed. In addition, a Gaussian-type pitch angle distribution function

$$f(\Lambda) = \exp\left[-\frac{(\Lambda - \Lambda_{peak})^2}{\Delta\Lambda^2}\right] \quad (8)$$

is assumed for the energetic particles, where  $\Lambda = \mu B_0/E$  is the pitch angle variable,

1  
2  
3 *Simulations of EP driven instabilities in CFQS: H. Wang, Y. Todo, J. Huang et al.* 6

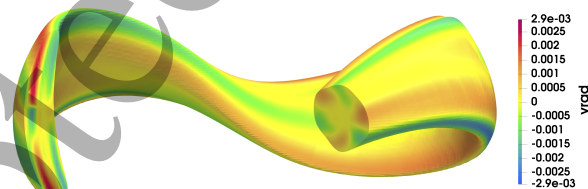
4  $\mu$  is the magnetic moment,  $E$  is the particle energy,  $\Lambda_{peak} = 0.1$  represents the pitch  
5 angle for the distribution peak, and  $\Delta\Lambda = 0.2$  is a parameter to control the distribution  
6 width. Since NBI system of the CFQS has not been equipped yet, the above  $\Lambda_{peak}$  and  
7  $\Delta\Lambda$  parameters are set by reference to the Large Helical Device[19].  
8

9  
10 The number of computational particles is 32 million. Cylindrical coordinates  
11  $(R, \phi, z)$  are employed. Different from the previous simplified cases[19, 22, 23], in order  
12 to explore all possible toroidal mode numbers, the present work models the entire plasma  
13 with a toroidal range from  $\phi = 0$  to  $\phi = 2\pi$ . The numbers of grid points in  $(R, \phi, z)$   
14 directions are (128, 256, 128), respectively.  
15  
16

### 17 3. Simulation results in the case with magnetic islands

#### 18 3.1. Mode profiles in both three and two-dimensional form

19  
20 The simulated mode profile of radial velocity  $v_{rad}$  is shown in Fig. 4. In the toroidal  
21 direction, only 3/4 tours are shown from  $\phi = 0$  to  $\phi = 1.5\pi$ . The plasma from  $\phi = 1.5\pi$   
22 to  $\phi = 2\pi$  is cut in order to better observe the poloidal cross section. The poloidal cross  
23 section on the left side is located at  $\phi = 0$ , while the one on the right side is located at  
24  $\phi = 1.5\pi$ . They are bean-shaped and triangular, respectively. In the radial direction,  
25 only the plasmas whose pressure is greater than 0.83 maximum are displayed. In other  
26 words, the  $v_{rad}$  is plotted on the constant pressure surface where  $P = 0.83P_{max}$ , or the  
27 surface where  $r/a = 0.4$ . This surface is important because  $v_{rad}$  is strong there. It is  
28 clear that the poloidal mode number  $m = 3$ . On the bean-shaped cross section,  $v_{rad}$  is  
29 stronger than that on the triangular one. This is the first time to show instability in  
30 the CFQS in three-dimensional form.  
31  
32  
33  
34  
35  
36  
37



38  
39  
40  
41  
42  
43  
44  
45 **Figure 4.** Radial velocity  $v_{rad}$  of the simulated mode in three-dimensional form. The  
46 orange and red represent the velocity from core to edge, while the green and blue  
47 represent the velocity from edge to core.  
48

49  
50 In order to better show the details of the velocity, its vortices at  $\phi = 0$  and  $\phi = 0.5\pi$   
51 are shown in Fig. 5. Whether it is on the bean-shaped cross section or on the triangular  
52 one, it is easy to find three clockwise vortices and three counterclockwise ones. This  
53 suggests that the poloidal mode number  $m = 3$ . It can also be seen that on the bean-  
54 shaped cross section, in the direction from the center to the upper and lower ends,  
55 the velocity is larger than that of other places, including both the bean-shaped and  
56 triangular cross sections. This is the reason why in Fig. 4 the color of the bean-shaped  
57  
58  
59  
60



cross section is stronger than that of the triangular one. The radial velocity  $v_{rad}$  is not toroidally symmetric.

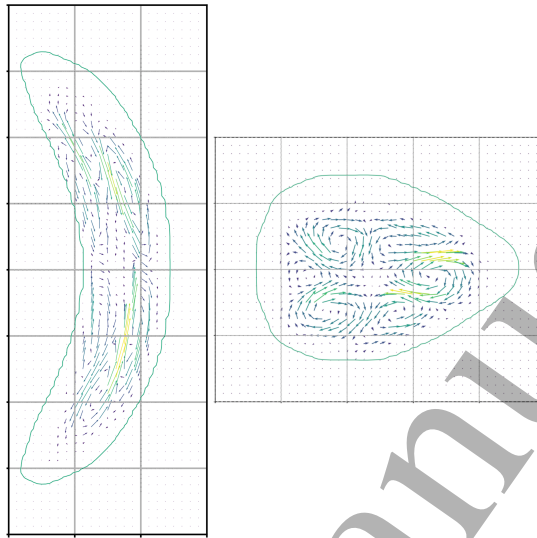


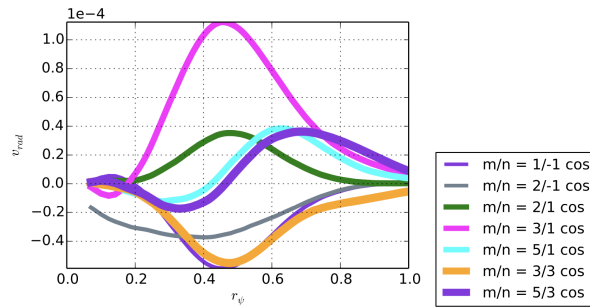
**Figure 5.** The velocity vortices at  $\phi = 0$  (beam-shaped cross section) and  $\phi = 0.5\pi$  (triangular cross section). The long red arrows represent a large velocity, while the short blue arrows represent a small velocity.

The mode profile in two-dimensional form is also analyzed, as shown in Fig. 6. All components with an absolute toroidal mode number less than 5 and a poloidal mode number less than 8 are analyzed. Only the strongest nine components are plotted; the remaining components are not plotted because they are weak. The dominant component is  $m/n = 3/1$ , as shown by the magenta line. The mode width is very large, and that means the simulated mode is a global one. The poloidal mode number agrees with those in Fig. 4 and Fig. 5. For the toroidal mode number, in addition to the  $n=1$  component, the  $n=-1$  and  $n=3$  components cannot be neglected. This suggests very strong toroidal mode coupling, which is difficult to see in a tokamak, but can be seen on some stellarators like the LHD but not very strongly. This mode coupling phenomenon has been theoretically analyzed by Don Spong[24]. The toroidal components  $n = n_0 + iN_{fp}$  are strong, where  $n_0$  is the dominant toroidal mode number and it is 1 for Fig. 6,  $i$  is an arbitrary integer and it is -1, 0, and 1 for Fig. 6,  $N_{fp}$  is the number of the field period and it is 2 for the CFQS. Strong mode coupling happens under the condition of a very small  $N_{fp}$ . In the LHD stellarator,  $N_{fp} = 10$  is relatively large, and thus the toroidal mode coupling is weak. The simulated mode coupling phenomenon in the present work is consistent with theoretical prediction[24] and also, it is similar to the simulation of the FAR3d code[8].

### 3.2. Mode frequency and growth rate

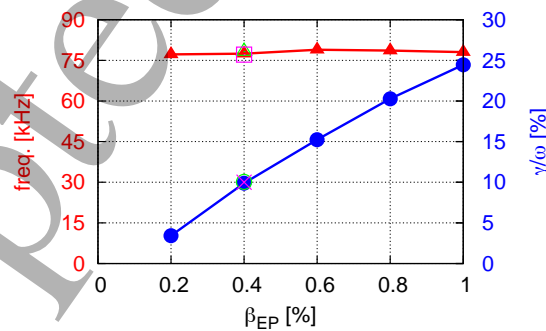
The dependence of mode frequency and growth rate on energetic particle beta  $\beta_{EP}$  (or energetic particle pressure) are analyzed, as shown in Fig. 7. The growth rate

1  
2  
3 *Simulations of EP driven instabilities in CFQS: H. Wang, Y. Todo, J. Huang et al* 8  
4



5  
6  
7  
8  
9  
10  
11  
12  
13  
14  
15 **Figure 6.** The mode profile of poloidal velocity  $v_{rad}$  in two-dimensional form.

16  
17  
18 increases with energetic particle pressure and this represents the simulated mode  
19 driven by energetic particles. This property is similar to that of Ref. [8]. But the  
20 mode frequency 79 kHz does not depend on energetic particles. It is close to the  
21 global Alfvén eigenmode (GAE) frequency[25]  $(n - m\iota) \times \omega_A / (2\pi) = 78$  kHz, where  
22  $\omega_A = v_A / R_0 = 6.147 \times 10^6$  rad/s, where  $v_A$  is Alfvén velocity,  $n = 1$ ,  $m = 3$ ,  
23  $\iota = 1/q = 0.36$ , and  $q$  is safety factor. This shows that the simulated mode is likely a  
24 GAE, or, an EPM located near the Alfvén continuum. In order to ensure the convergence  
25 of the simulation, different numbers of computational particles are loaded to compare  
26 with the usual results. In Fig. 7, closed triangles and closed circles are calculated with  
27 32 million computational particles. At  $\beta_{EP} = 0.4\%$ , different numbers of computational  
28 particles are loaded, as shown by the open square and cross (8 million), and the open  
29 triangle and open circle (64 million). The points obtained under different computational  
30 particle numbers are consistent with each other, which confirms good convergence in the  
31 simulation.  
32  
33  
34  
35  
36  
37



38  
39  
40  
41  
42  
43  
44  
45  
46  
47  
48  
49  
50 **Figure 7.** The dependence of mode frequency (triangles) and growth rate (circles)  
51 on energetic particle pressure. Closed triangles and closed circles are calculated with  
52 32 million computational particles, the open square and cross are calculated with 8  
53 million computational particles, and the open triangle and open circle are calculated  
54 with 64 million computational particles.  
55

56  
57 The time evolutions of different harmonics were also checked carefully. The  
58 frequencies of those harmonics were the same, but amplitudes were different. This  
59 shows that these harmonics constitute the same eigenmode.  
60

Normally, NBI energy  $E_{NBI}$  is difficult to change, and thus, it is not necessary to scan the parameter  $E_{NBI}$ . But sometimes, in order to better understand the mode properties, it is still useful to investigate the mode behavior under different  $E_{NBI}$  parameters. The dependence of mode frequency and growth rate on  $E_{NBI}$  is analyzed, as shown in Fig. 8(a). The mode frequency does not depend on NBI energy. Growth rates in the cases of  $E_{NBI} \leq 30 \text{ keV}$  are not plotted. The noises in these cases are too strong to accurately estimate the growth rate. But it is clear that the growth rates in these cases are apparently smaller than those in other cases. For the  $E_{NBI} = 10 \text{ keV}$  case, the mode is stable.

The parallel velocities of resonant particles can be evaluated by analyzing energy transfer in  $\Lambda$  and  $E$  phase space. Roughly,  $v_{\parallel} = \sqrt{1 - \Lambda} \sqrt{2E/m_{EP}}$ , where  $m_{EP}$  is the energetic particle mass. The ratio of  $v_{\parallel}$  to  $v_A$  is shown in Fig. 8(b). The parallel velocities of resonant particles are close to  $1/3v_A$ , consistent with the AE destabilization condition[26]. This implies that the simulated mode may be an Alfvén eigenmode, or, an EPM located near the Alfvén continuum.

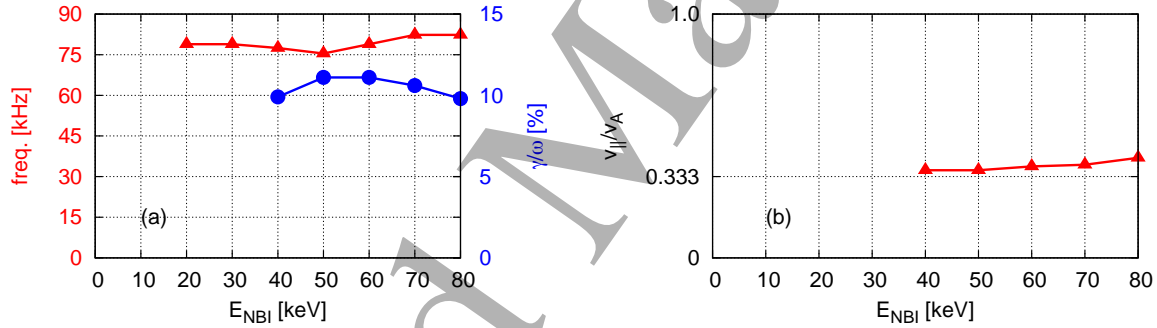


**Figure 8.** The dependence of (a) mode frequency (triangles) and growth rate (circles) and (b) the parallel velocity of resonant particles on NBI energy  $E_{NBI}$ .

The dependence of mode frequency and growth rate on the peak value of energetic particle pitch angle  $\Lambda_{peak}$  is also analyzed, but the conclusion is not clear. When changing  $\Lambda_{peak}$ , another mode appears and it has a strong influence on the present  $m/n = 3/1$  mode. As a result, no clear trend is seen in the  $3/1$  mode, either in frequency or in growth rate. The phenomenon of multi-mode coexistence is very interesting, but it will not be discussed in this paper, but in another one.

### 3.3. Alfvén continuum

In order to identify the simulated mode, the Alfvén continuum is plotted in Fig. 9. This figure is analyzed using the STELLGAP code[24], which was developed for shear Alfvén continua in stellarators. In the present work, the STELLGAP code (version 7[27]) with sound wave coupling effects is conducted for analysis. The figure does not show data with a frequency that exceeds 200 kHz. Considering that the frequency of the simulated mode is only 79 kHz, the range of the vertical axis is reasonable. All components with an

*Simulations of EP driven instabilities in CFQS: H. Wang, Y. Todo, J. Huang et al* 10

absolute toroidal mode number less than 4 and a poloidal mode number less than 10 are analyzed. But in the frequency range below 200 kHz, only three branches can be shown, and the other branches are outside this range. As calculated above, the frequency of the simulated mode is close to the GAE frequency. But near the mode location, there is not any extreme value of the  $m/n = 3/1$  continuum. Considering the mode intersects with the continuum, it may be an EPM-like mode.

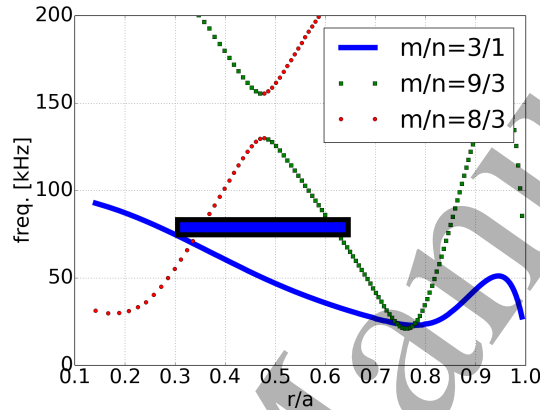


**Figure 9.** The Alfvén continuum in the case with magnetic islands.

### 3.4. Resonant condition

The simulated mode is driven by energetic particles through resonant interactions, and the frequency of mode, the frequency of toroidal motion  $f_\phi$ , and the frequency of poloidal motion  $f_\theta$  must satisfy the following resonant condition:

$$f_{mode} = n f_\phi - l f_\theta, \quad (9)$$

where  $f_{mode}$  is the mode frequency,  $n$  is the toroidal mode number, and  $l$  is an arbitrary integer[12, 28]. The resonant condition in Eq. (9) is general for toroidal plasmas, especially for tokamak plasmas. In the stellarator, there is a stronger theorem as follows[29]:

$$f_{mode} = N f_\phi - L f_\theta, \quad (10)$$

where  $N = n + j\nu N_{fp}$ ,  $L = m + j\mu$ ,  $j = 0, \pm 1$ ,  $\nu$  and  $\mu$  are arbitrary integers. The resonances with non-zero  $j$  values are caused by the absence of axial symmetry and they are not often observed, even in stellarators. In order to analyze the resonant condition, 4096 particles with maximum  $\delta f$  values are marked and traced. The time for each particle to pass one round in the toroidal angle is defined as the toroidal period  $T_\phi$ , and accordingly, a frequency  $f_\phi = 1/T_\phi$ . Similarly, in the poloidal direction,  $T_\theta$  and  $f_\theta$  are defined. In order to reduce the error, after the 4096 particles were marked, they were continuously traced for about 0.9 ms (about 70 mode periods) to calculate the average value of  $f_\phi$  and  $f_\theta$ . As a result, the relationship of particle frequencies  $f_\phi$  and

*Simulations of EP driven instabilities in CFQS: H. Wang, Y. Todo, J. Huang et al 11*

$f_\theta$  is plotted in Fig. 10(a). The solid green line representing  $f_\phi = 2.33f_\theta + 26.33$  kHz or  $f_{mode} = 3f_\phi - 7f_\theta$  passes through most of the red dots. The dotted blue line representing  $f_\phi = 2f_\theta + 79$  kHz or  $f_{mode} = f_\phi - 2f_\theta$  also passes through many red dots. Since the solid green line fits the red dots better than the dotted blue line, it confirms that  $n = 1$ ,  $j = 1$ ,  $\nu = 1$ ,  $m = 3$ ,  $\mu = 4$ , and  $L = 7$  in Eq. (10) are dominant for the simulated mode. The resonance of  $j = 1$  becomes dominant, which is caused by the absence of axial symmetry. More specifically, in the CFQS, this is caused by the 2-fold rotational symmetry of the equilibrium magnetic field. In addition, although the distribution ranges of  $f_\phi$  and  $f_\theta$  are wide, the distribution width in the direction perpendicular to the green line is still narrow, which shows that the data is reliable. The dashed pink line representing  $f_\phi = f_\theta + 79$  kHz or  $f_{mode} = f_\phi - f_\theta$  passes through a few red dots located at a low energy region where  $f_\theta \approx 45$  kHz and  $f_\phi \approx 125$  kHz. This suggests that  $n = 1$ ,  $j = 0$ , and  $L = 1$  in Eq. (9) are subdominant for the simulated mode. Particles satisfying various resonant conditions appear simultaneously. The  $L$  value in Eq. (10) is directly shown in Fig. 10(b) for  $n = 1$ ,  $j = 1$ , and  $L = 7$ . They are also shown in Fig. 10(c) for  $n = 1$ ,  $j = 0$  and  $L = 1$ . In Fig. 10(b), most particles are located around  $L = 7$ , while in Fig. 10(c), many particles are located around  $L = 2$  but the bias is relatively large, especially in the low  $f_\theta$  region. This confirms again that  $n = 1$ ,  $j = 1$ , and  $L = 7$  in Eq. (10) are dominant for the simulated mode. In Fig. 10(c), a few particles are perfectly located at  $L = 1$ . This confirms again that in Eq. (9)  $n = 1$ ,  $j = 0$ , and  $L = 1$  are subdominant.

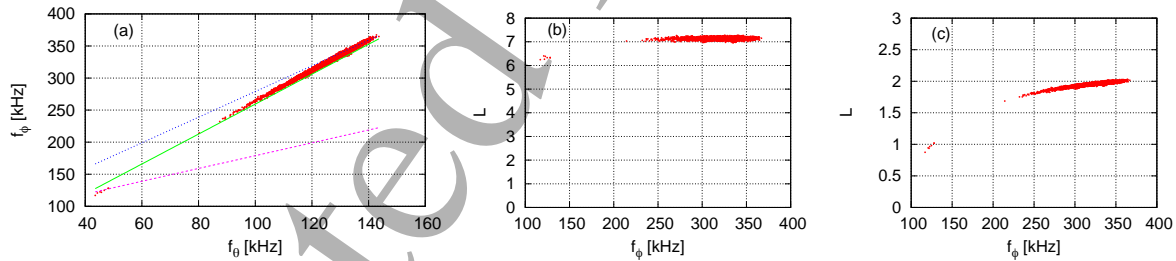


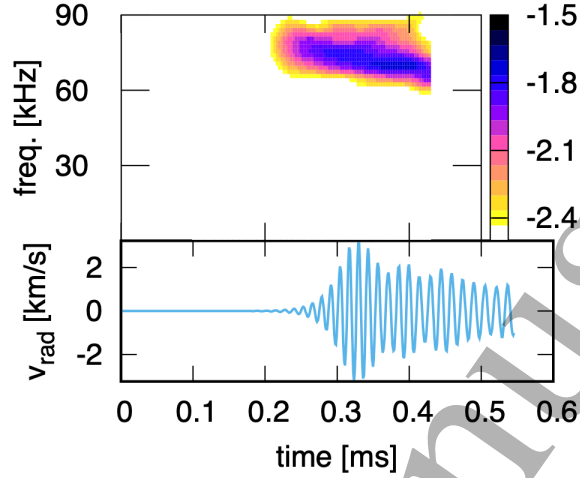
**Figure 10.** (a) The relationship of particle frequencies  $f_\phi$  and  $f_\theta$  of 4096 particles with maximum  $\delta f$  values. The solid green line represents  $f_{mode} = 3f_\phi - 7f_\theta$ , the dotted blue line represents  $f_{mode} = f_\phi - 2f_\theta$ , and the dashed pink line represents  $f_{mode} = f_\phi - f_\theta$ . (b) The  $L$  values of 4096 resonant particles for  $n = 1$  and  $j = 1$ . (c) The  $L$  values of 4096 resonant particles for  $n = 1$  and  $j = 0$ .

### 3.5. Nonlinear frequency chirping and hole-clump formation in phase space

All of the above analysis is carried out in the linear growth phase. In this subsection, the mode time evolution and frequency spectrum in both linear growth phase and nonlinear saturated phase are investigated, as shown in Fig. 11. The mode frequency in the linear growth phase is 79 kHz. At  $t = 0.32$  ms, the mode amplitude becomes maximum, and then the mode steps into a nonlinear saturated phase and the mode frequency starts

1  
2  
3 *Simulations of EP driven instabilities in CFQS: H. Wang, Y. Todo, J. Huang et al 12*

4 to chirp down. After about 0.1 ms, the mode frequency has already chirped down to  
5 70 kHz. This is the first time to show frequency chirping in the CFQS.  
6  
7



24 **Figure 11.** The time evolution of (top) frequency spectrum and (bottom) radial  
25 velocity  $v_{rad}$ . Both panels share the horizontal axis. The color bar indicates the  
26 magnitude in logarithmic scale.  
27

28  
29 The energetic particle energy transfer  $\delta f \times dE/dt$  of all simulation particles is  
30 analyzed in the phase space of pitch angle  $\Lambda$  and energy  $E$ , as shown in Fig. 12. The  
31  $\delta f \times dE/dt$  is mainly marked in purple, which represents  $\delta f \times dE/dt < 0$ , energy transfers  
32 from energetic particles to the mode, and it is destabilized. The five curves represent  
33 constant resonance frequencies  $f_{res}$ , which are evaluated by  $f_{res} = kf_{\theta Approx}$ . The  
34 constant  $k$  is a coefficient.  $f_{\theta Approx} = \sqrt{1 - \Lambda} \sqrt{2E/m_{EP}/(2\pi qR_0)}$  is the approximate  
35 poloidal frequency calculated from the values of  $\Lambda$  and  $E$ . In ideal case with zero orbit  
36 width,  $f_{\phi} = qf_{\theta}$ , then,  $f_{res} = kf_{\theta}$  where  $k = Nq - L$ . In the realistic case,  $f_{\phi}$  is not  
37 simply  $qf_{\theta}$ , and  $f_{res}$  can not be simply shown in  $(\Lambda, E)$  space, but  $f_{res}$  can be roughly  
38 evaluated in a statistical way. In Fig. 10, 4096 particles were investigated and their  
39 resonance frequencies, energies, and pitch angles are known. The coefficient  $k = 0.586$   
40 can be obtained by plotting 4096 particles and curve fitting in a figure of  $f_{res}$  versus  
41  $f_{\theta Approx}$ . From bottom to top, these five curves represent  $f_{res} = 50$  kHz, 60 kHz,  
42 80 kHz, and 90 kHz, respectively. Although constant  $f_{res}$  curves calculated in this figure  
43 are not as exact as those in Fig. 10, they are still good references for observing frequency  
44 changes. In the left subfigure, the purple part is located around  $f_{res} = 75$  kHz. While  
45 in the right subfigure, the location of the purple part changes, and it is located around  
46  $f_{res} = 65$  kHz. The purple part moves from the high frequency region to the low  
47 frequency one during mode frequency chirping down.  
48  
49  
50  
51  
52  
53

54 The energetic particle distribution  $\delta f$  of all simulation particles is also analyzed  
55 in  $(\Lambda, E)$  space, as shown in Fig. 13. The blue color represents  $\delta f < 0$  (hole) while  
56 the red color represents  $\delta f > 0$  (clump). The  $\delta f$  distribution is integrated over the  
57 whole simulation domain. In the left subfigure, the hole is located on the blue curve  
58 representing  $f_{res} = 80$  kHz, and the center of the hole region is slightly above the  
59  
60

Simulations of EP driven instabilities in CFQS: H. Wang, Y. Todo, J. Huang et al 13

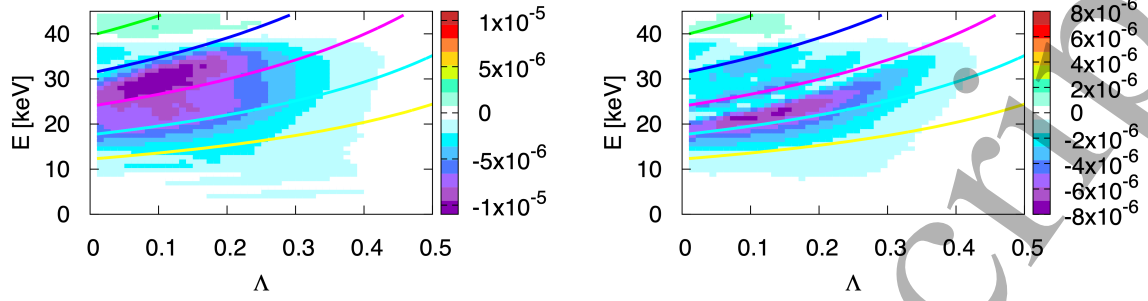


**Figure 12.** The energetic particle energy transfer  $\delta f \times dE/dt$  in  $(\Lambda, E)$  space at (left)  $t = 0.34$  ms and (right)  $t = 0.50$  ms. The five curves represent constant  $f_{res}$  curves from 50 kHz to 90 kHz.

blue curve. While in the right subfigure, the center of the hole region moves slightly rightward, and just below the blue curve. The hole structure moves slightly from the high frequency region to the low frequency one during mode frequency chirping down. The clump frequency also slightly decreases. In the left subfigure, the center of the clump region is located slightly above the  $f_{res} = 60$  kHz curve, while in the right subfigure, it is located between  $f_{res} = 50$  kHz and  $f_{res} = 60$  kHz. The movement of hole and clump indicates that the particles comprising the hole and clump are kept resonant with the mode during the frequency chirping. In Fig. 13, there is another hole-clump pair in the low energy region where  $E < 10$  keV. By mapping the 4096 particles of Fig. 10 into  $(\Lambda, E)$  space, it is easy to identify that in Fig. 13 the particles in the large hole-clump pair (or in the high energy region) satisfy the resonant condition with  $j = 1$ , while the particles in the small hole-clump pair (or in the low energy region) satisfy the resonant condition with  $j = 0$ . Again, particles satisfying various resonant conditions appear simultaneously.

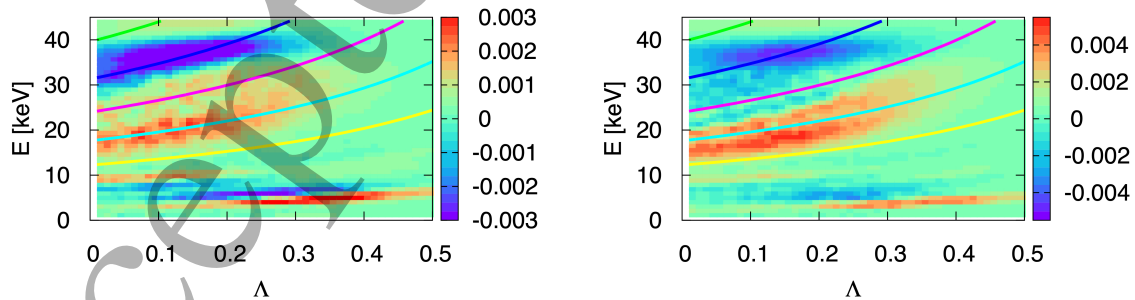
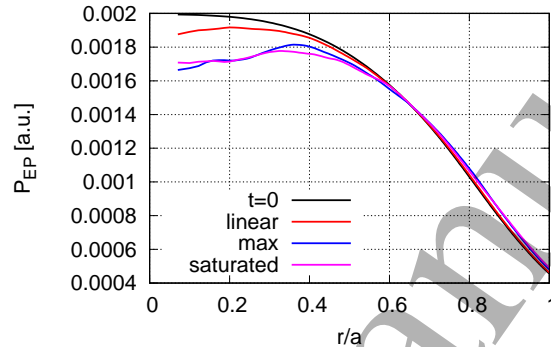


**Figure 13.** The energetic particle distribution  $\delta f$  in  $(\Lambda, E)$  space at (left)  $t = 0.34$  ms and (right)  $t = 0.50$  ms. The five curves represent constant  $f_{res}$  curves from 50 kHz to 90 kHz.

1  
2  
3 *Simulations of EP driven instabilities in CFQS: H. Wang, Y. Todo, J. Huang et al 14*

4  
5 *3.6. Energetic particle radial transport*

6  
7 Energetic particle radial transport can be seen from the change of the energetic particle  
8 pressure profile, and thus, the energetic particle pressure profiles at different times are  
9 plotted in Fig. 14. Compared with that in the initial phase, the energetic particle  
10 pressure in the core region is reduced by about 15% at the moment of maximum mode  
11 amplitude. This indicates strong energetic particle radial transport.

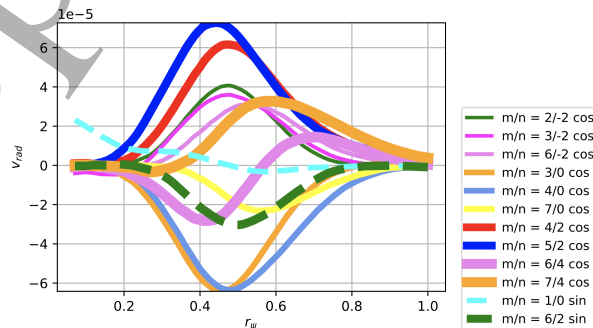


12  
13  
14  
15  
16  
17  
18  
19  
20  
21  
22  
23  
24  
25  
26  
27 **Figure 14.** The energetic particle pressure profiles of the mode in the initial and linear  
28 growth phases, at the moment of maximum amplitude, and in the nonlinear saturated  
29 phase.

30  
31  
32  
33 **4. Simulation results in the case without magnetic island**

34  
35 *4.1. Mode profiles*

36  
37 The mode profile is analyzed and shown in Fig. 15. Similar to that in Fig. 6, only the  
38 strongest twelve components are plotted. The dominant component is  $m/n = 5/2$ . For  
39 the toroidal mode number, in addition to the  $n = 2$  component, the  $n = -2$ ,  $n = 0$ ,  
40 and  $n = 4$  components cannot be neglected. Similar to that in Fig. 6, this suggests very  
41 strong toroidal mode coupling which is difficult to see in a tokamak.



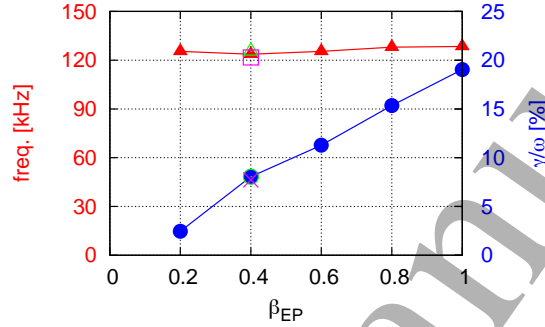
42  
43  
44  
45  
46  
47  
48  
49  
50  
51  
52  
53  
54  
55  
56 **Figure 15.** The mode profile of poloidal velocity  $v_{rad}$  in the case without magnetic  
57 island.  
58  
59  
60



1  
2  
3 *Simulations of EP driven instabilities in CFQS: H. Wang, Y. Todo, J. Huang et al 15*

4  
5 *4.2. Mode frequency and growth rate*

6  
7 The dependence of mode frequency and growth rate on energetic particle beta  $\beta_{EP}$   
8 (or energetic particle pressure) are analyzed, as shown in Fig. 16. Similar to that in  
9 Fig. 7, the growth rate increases with energetic particle pressure which represents that  
10 the simulated mode is driven by energetic particles. But the mode frequency 125 kHz  
11 does not depend on energetic particles.  
12  
13



14  
15  
16  
17  
18  
19  
20  
21  
22  
23  
24  
25  
26  
27 **Figure 16.** The dependence of mode frequency (triangles) and growth rate (circles)  
28 on energetic particle pressure. Closed triangles and closed circles are calculated with  
29 32 million computational particles, the open square and cross are calculated with 8  
30 million computational particles, and the open triangle and open circle are calculated  
31 with 64 million computational particles.  
32

33  
34 Similar to that in Sec. 3, the frequencies of different harmonics are the same,  
35 but amplitudes are different. This shows that these harmonics constitute the same  
36 eigenmode.

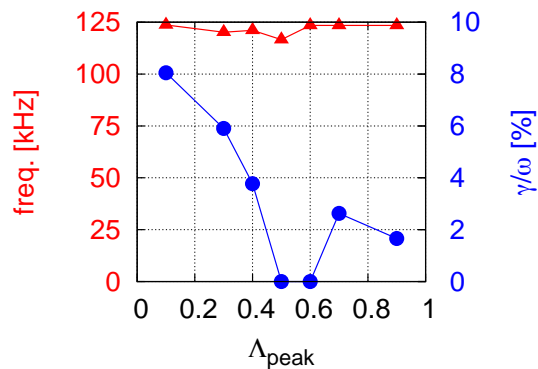
37  
38 The dependence of mode frequency and growth rate on  $E_{NBI}$  is also analyzed. For  
39 the cases where  $E_{NBI} \leq 20$  keV and those where  $E_{NBI} \geq 70$  keV, the mode is stable.  
40 For the cases where  $30 \text{ keV} \leq E_{NBI} \leq 60$  keV, the mode frequency does not depend on  
41 NBI energy.  
42

43  
44 The dependence of mode frequency and growth rate on the peak value of energetic  
45 particle pitch angle  $\Lambda_{peak}$  is also analyzed, as shown in Fig. 17. The mode frequency  
46 125 kHz does not depend on  $\Lambda_{peak}$ . The growth rate decreases with the increasing of  
47  $\Lambda_{peak}$ , except those points at  $\Lambda_{peak} = 0.5$  and  $\Lambda_{peak} = 0.6$ . At those points, the mode  
48 keeps stable. The stabilization may be cause by the transition from the passing particles  
49 to the trapped particles. According to this figure, in order to suppress the simulated  
50 mode, it is better not to inject the neutral beam tangentially.  
51  
52

53  
54 *4.3. Alfvén continuum*

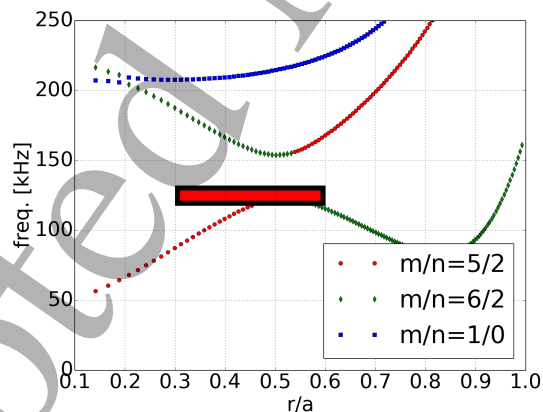
55  
56 From the above analysis, it can be seen that the simulated mode is very likely to be  
57 an Alfvén eigenmode. At  $\iota \approx 0.3636$  or  $\iota \approx \frac{2}{(5+6)/2}$ , indeed, a TAE with  $m/n = 5/2$   
58 and  $m/n = 6/2$  is possible to be excited. For better analysis, the Alfvén continuum  
59 is plotted using the STELLGAP code in Fig. 18. The harmonics  $m/n = 5/2$  and  
60

1  
2  
3 *Simulations of EP driven instabilities in CFQS: H. Wang, Y. Todo, J. Huang et al 16*



18 **Figure 17.** The dependence of mode frequency (circle) and growth rate (triangle) on  
19 the peak value of energetic particle pitch angle  $\Delta_{peak}$ .

21  
22  $m/n = 6/2$  constitute a gap, and the simulated 5/2 mode is just below the gap. The  
23 STELLGAP code is conducted based on the VMEC equilibrium, but the MEGA code is  
24 conducted based on the HINT equilibrium. Considering the differences between VMEC  
25 and HINT (or the differences between STELLGAP and MEGA), the mode may be  
26 located inside but not below the gap. Thus, the simulated mode may be the toroidal  
27 Alfvén eigenmode (TAE).  
28  
29  
30



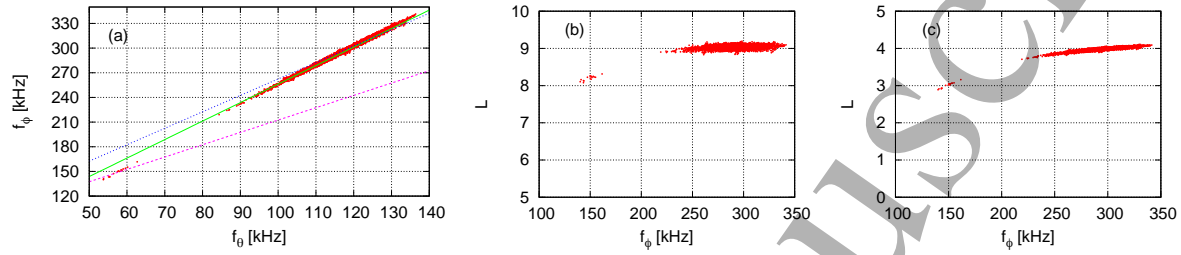
31  
32 **Figure 18.** The Alfvén continuum in the case without magnetic island.

#### 33 4.4. Resonant condition

34  
35 In order to analyze the resonant condition, similar to that in Sec. 3, 4096 particles with  
36 maximum  $\delta f$  values were analyzed. The relationship of particle frequencies  $f_\phi$  and  $f_\theta$  is  
37 plotted in Fig. 19(a). The solid green line representing  $f_{mode} = 4f_\phi - 9f_\theta$  perfectly passes  
38 through most of these red dots. The dotted blue line representing  $f_{mode} = 2f_\phi - 4f_\theta$   
39 also passes through many red dots. Again, the resonance of  $j = 1$  becomes dominant,  
40 which is caused by the 2-fold rotational symmetry of the equilibrium magnetic field. The  
41  
42  
43  
44  
45  
46  
47  
48  
49  
50  
51  
52  
53  
54  
55  
56  
57  
58  
59  
60

1  
2  
3 *Simulations of EP driven instabilities in CFQS: H. Wang, Y. Todo, J. Huang et al 17*

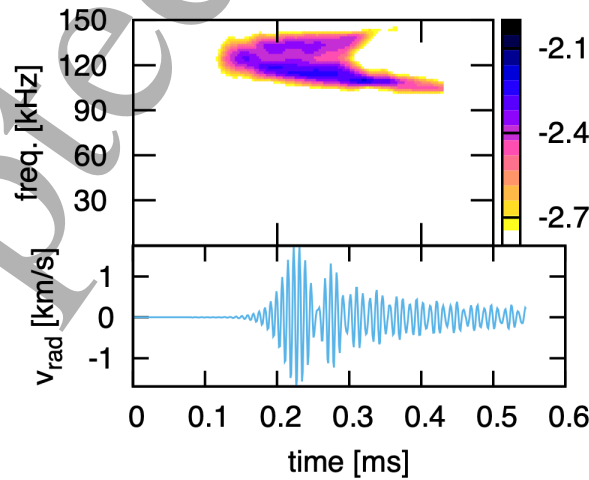
4 dashed pink line representing  $f_{mode} = 2f_\phi - 3f_\theta$  passes through a few red dots located at  
5 the low energy region where  $f_\theta \approx 55$  kHz and  $f_\phi \approx 145$  kHz. Particles satisfying various  
6  $j$  values of the resonant condition appear simultaneously. The  $L$  values in Eq. (10) are  
7 directly shown in Fig. 19(b) for  $n = 2$ ,  $j = 1$  and  $L = 9$ . They are also shown in  
8 Fig. 19(c) for  $n = 2$ ,  $j = 0$  and  $L = 4$ .



22 **Figure 19.** (a) The relationship of particle frequencies  $f_\phi$  and  $f_\theta$  of 4096 particles  
23 with maximum  $\delta f$  values. The solid green line represents  $f_{TAE} = 4f_\phi - 9f_\theta$ , the  
24 dotted blue line represents  $f_{TAE} = 2f_\phi - 4f_\theta$ , and the dashed pink line represents  
25  $f_{TAE} = 2f_\phi - 3f_\theta$ . (b) The  $L$  values of 4096 resonant particles for  $n = 2$  and  $j = 1$ .  
26 (c) The  $L$  values of 4096 resonant particles for  $n = 2$  and  $j = 0$ .

27  
28  
29  
30 *4.5. Nonlinear frequency chirping and hole-clump formation in phase space*

31 In this subsection, the mode time evolution and frequency spectrum in both linear  
32 growth and nonlinear saturated phases are investigated, as shown in Fig. 20. The  
33 dominant branch chirps down to 105 kHz, while another branch chirps up to 140 kHz  
34 but it is weak.  
35  
36

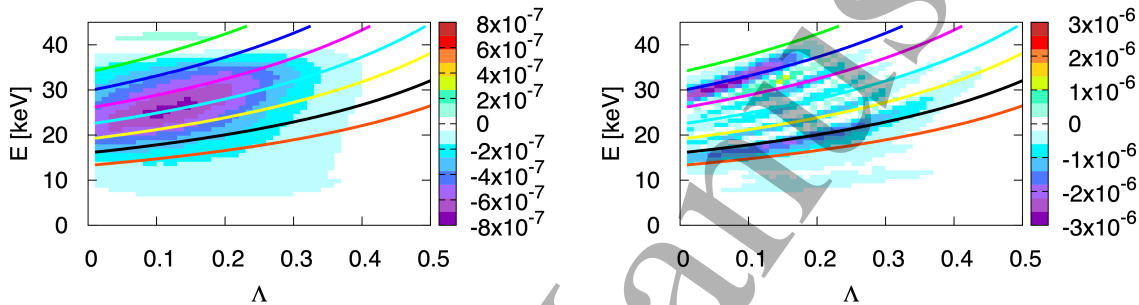


53 **Figure 20.** The time evolution of (top) frequency spectrum and (bottom) radial  
54 velocity  $v_{rad}$ . Both panels share the horizontal axis. The color bar indicates the  
55 magnitude in logarithmic scale.  
56

57  
58 The energetic particle energy transfer  $\delta f \times dE/dt$  of all simulation particles is  
59 analyzed in the phase space of pitch angle  $\Lambda$  and energy  $E$ , as shown in Fig. 21.  
60

1  
2  
3 *Simulations of EP driven instabilities in CFQS: H. Wang, Y. Todo, J. Huang et al 18*

4 Similar to that in the EPM-like mode case, the seven curves represent  $f_{res} = kf_{\theta Approx}$   
5 where  $k = 1.126$ . At  $t = 0.19$  ms, the  $\delta f \times dE/dt$  is mainly negative, and the TAE  
6 is destabilized. Those particles that provide energy for the TAE are mainly located  
7 around  $f_{res} = 130$  kHz. At  $t = 0.36$  ms, the  $\delta f \times dE/dt$  is still mainly negative, but  
8 the purple part is split into two independent parts. These two parts are located around  
9  $f_{res} = 150$  kHz and  $f_{res} = 110$  kHz, and they correspond to the high and low frequency  
10 branches of the TAE in Fig. 20. The two purple parts move during the frequency  
11 chirping of the two branches of the TAE.  
12  
13  
14  
15



27 **Figure 21.** The energetic particle energy transfer  $\delta f \times dE/dt$  in  $(\Lambda, E)$  space at (left)  
28  $t = 0.19$  ms and (right)  $t = 0.36$  ms. The seven curves represent constant  $f_{\theta}$  curves or  
29 constant  $f_{res}$  curves from 100 kHz to 160 kHz.  
30

31  
32 The energetic particle distribution  $\delta f$  of all simulation particles is also analyzed  
33 in  $(\Lambda, E)$  space, as shown in Fig. 22. At  $t = 0.19$  ms, the hole is located around  
34  $f_{res} = 135$  kHz. While at  $t = 0.36$  ms, the hole moves upward to  $f_{res} = 150$  kHz. Also,  
35 at  $t = 0.19$  ms, the clump is located around  $f_{res} = 125$  kHz, while at  $t = 0.36$  ms, the  
36 clump moves downward to  $f_{res} = 105$  kHz. The movement of hole and clump indicates  
37 that the particles comprising them are kept resonant with the TAE during the frequency  
38 chirping. In Fig. 22, there is another hole-clump pair in the low energy region where  
39  $E \approx 10$  keV. In Fig. 22 the particles in the large hole-clump pair (or in the high energy  
40 region) satisfy the resonant condition with  $j = 1$ , while the particles in the small hole-  
41 clump pair (or in the low energy region) satisfy the resonant condition with  $j = 0$ .  
42  
43  
44  
45  
46  
47

#### 48 4.6. Energetic particle radial transport

49 Similar to that in Fig. 14, the energetic particle pressure profiles at different times are  
50 plotted in Fig. 23, to see the energetic particle radial transport. Compared with that  
51 in the initial phase, the energetic particle pressure in the core region is reduced by  
52 about 7% at the moment of maximum TAE mode amplitude. Comparing Fig. 14 and  
53 Fig. 23, it can be seen that the transport caused by the EPM-like mode in the present  
54 simulation is stronger. The difference between Fig. 14 and Fig. 23 can be explained  
55 by the following reasons. First, in the present simulations, both the TAE growth rate  
56 and TAE maximum amplitude are weaker than that of the EPM-like mode. Second,  
57  
58  
59  
60

Simulations of EP driven instabilities in CFQS: H. Wang, Y. Todo, J. Huang et al 19

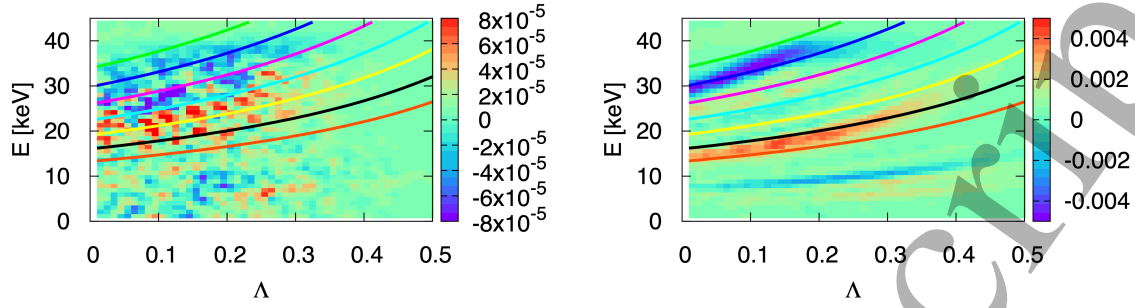


**Figure 22.** The energetic particle distribution  $\delta f$  in  $(\Lambda, E)$  space at (left)  $t = 0.19$  ms and (right)  $t = 0.36$  ms. The seven curves represent constant  $f_\theta$  curves or constant  $f_{res}$  curves from 100 kHz to 160 kHz.

energetic particles are initially loaded at  $t = 0$ , and after that, energetic particles are continuously transported with time. In Fig. 14, the mode amplitude becomes maximum at  $t = 0.32$  ms, while in Fig. 23 the mode amplitude becomes maximum at  $t = 0.19$  ms. The analysis of the EPM-like mode in Fig. 14 is significantly later than that of the TAE in Fig. 23, and more particles are transported.

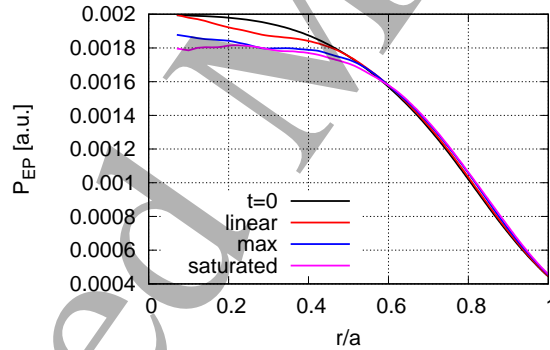


**Figure 23.** The energetic particle pressure profiles of the TAE in the initial and linear growth phases, at the moment of maximum amplitude, and in the nonlinear saturated phase.

## 5. Summary

In summary, the nonlinear simulations of energetic particle driven instabilities in the CFQS are conducted using the MEGA code for the first time. The simulation parameters are based on the CFQS design. Two equilibria with and without magnetic islands are considered. The instability in the CFQS in three-dimensional form is shown for the first time. Both the EPM-like mode and TAE are found in the CFQS with and without magnetic islands. The dominant mode numbers are  $m/n = 3/1$  for the EPM-like mode and  $m/n = 5/2$  for the TAE. Strong mode coupling is found under the condition of a very low number of field period  $N_{fp}$  value. This result is consistent with theoretical

*Simulations of EP driven instabilities in CFQS: H. Wang, Y. Todo, J. Huang et al* 20

prediction[24], and it is similar to the simulation of the FAR3d code[8]. For the EPM-like mode, the mode frequency 79 kHz does not depend on energetic particle pressure or energetic particle beam velocity, while the growth rate increases with energetic particle pressure, and the growth rate is maximum for the energetic particle beam velocity of  $0.5v_A$ . For the TAE, similarly, the mode frequency 125 kHz does not depend on energetic particle pressure, energetic particle beam velocity, or the peak value of energetic particle pitch angle. The growth rate increases with energetic particle pressure, roughly decreases with the increasing of the peak value of energetic particle pitch angle, and the growth rate is maximum for the energetic particle beam velocity of  $0.5v_A$ . For the EPM-like mode, the resonant condition  $f_{mode} = 3f_\phi - 7f_\theta$  is dominant and  $f_{mode} = f_\phi - f_\theta$  is subdominant. For the TAE, the resonant condition  $f_{mode} = 4f_\phi - 9f_\theta$  is dominant and  $f_{mode} = 2f_\phi - 3f_\theta$  is subdominant. The 2-fold rotational symmetry of the equilibrium magnetic field plays important roles in the resonances of both modes. This kind of resonance is not often observed, even in stellarators. Also, the mode frequencies chirp in the nonlinear saturated phase. Hole and clump structures are formed in the pitch angle and energy phase space. The particles comprising the hole and clump are kept resonant with the modes during the mode frequencies chirping. Finally, during the mode activities, energetic particles are transported from the core region. For the present simulation, the transport caused by the EPM-like mode is stronger than that of the TAE.

For the CFQS operation, it should be noted that even if the  $\iota$  profile is only slightly changed, the properties of the instability may be greatly affected. For example, the excited mode changes from the EPM-like mode to the TAE. This conclusion is similar to that of Ref. [8]. In addition, in order to reduce or even completely suppress the EPM-like mode or TAE, it is worth trying to adjust the energetic particle beam velocity or the beam injection angle. Another possible way is to change the  $v_A$  by adjusting the magnetic field strength or plasma density, so that the energetic particle velocity avoids values around  $0.5v_A$ .

The present research leaves some interesting gaps. During the change of  $\Lambda_{peak}$ , in the case with magnetic islands, the phenomenon of multi-mode coexistence occurs. How these modes interact is an interesting subject. In the case without a magnetic island, the TAE is stable around  $\Lambda_{peak} \approx 0.5$ , and the reason is still unclear. In addition, the Alfvén-sound coupling was found in W7-AS[30], but it has not been discussed in CFQS. The above gaps may be filled in future work.

## Acknowledgments

Numerical computations were performed on the ‘‘Plasma Simulator’’ (NEC SX-Aurora TSUBASA) of National Institute for Fusion Science (NIFS) with the support and under the auspices of the NIFS Collaboration Research program (NIFS19KNXN397, NIFS20KNST156, NIFS21KNST196, and NIFS22KIST025), the JFRS-1 supercomputer system at Computational Simulation Centre of International Fusion Energy Research

## REFERENCES

21

Centre (IFERC-CSC), and the Supercomputer Fugaku provided by the RIKEN Center for Computational Science (Project IDs: hp200127, hp210178). This work was partly supported by MEXT as “Program for Promoting Researches on the Supercomputer Fugaku (Exploration of burning plasma confinement physics, JPMXP1020200103)”, JSPS KAKENHI Grant No. JP18K13529, No. JP18H01202, and “PLADyS”, JSPS Core-to-Core Program, A. Advanced Research Networks. The authors thank Dr. D. Spong of ORNL for kindly providing the STELLGAP code. Also, the authors thank Prof. Y. Xu of SWJTU, Prof. M. Isobe of NIFS, Prof. S. Okamura of NIFS, Prof. K. Nagasaki of Kyoto Univ., Dr. J. Huang of SWJTU, Dr. J. Wang of NIFS, Dr. M. Idoukass of NIFS, Prof. G. Fu of ZJU, and Mr. H. Li of Univ. Tokyo for their sincere help and fruitful discussions.

## References

- [1] Xu Y 2016 *Matter and Radiation at Extremes* **1** 192–200
- [2] OKAMURA S, MATSUOKA K, NISHIMURA S, ISOBE M, SUZUKI C, SHIMIZU A, NOMURA I, IDA K, FUJISAWA A, MURAKAMI S, NAKAJIMA N and YOKOYAMA M 2002 *Journal of Plasma and Fusion Research* **78** 166–179
- [3] Nelson B, Berry L, Brooks A, Cole M, Chrzanowski J, Fan H M, Fogarty P, Goranson P, Heitzenroeder P, Hirshman S, Jones G, Lyon J, Neilson G, Reiersen W, Strickler D and Williamson D 2003 *Fusion Engineering and Design* **66-68** 169–174 ISSN 0920-3796 22nd Symposium on Fusion Technology
- [4] SHIMIZU A, LIU H, ISOBE M, OKAMURA S, NISHIMURA S, SUZUKI C, XU Y, ZHANG X, LIU B, HUANG J, WANG X, LIU H, TANG C and the CFQS Team 2018 *Plasma and Fusion Research* **13** 3403123
- [5] ISOBE M, SHIMIZU A, LIU H, LIU H, XIONG G, YIN D, OGAWA K, YOSHIMURA Y, NAKATA M, KINOSHITA S, OKAMURA S, TANG C, XU Y and the CFQS Team 2019 *Plasma and Fusion Research* **14** 3402074
- [6] Liu H, Shimizu A, Xu Y, Okamura S, Kinoshita S, Isobe M, Li Y, Xiong G, Wang X, Huang J, Cheng J, Liu H, Zhang X, Yin D, Wang Y, Murase T, Nakagawa S and Tang C 2020 *Nuclear Fusion* **61** 016014
- [7] Wang X, Xu Y, Shimizu A, Isobe M, Okamura S, Todo Y, Wang H, Liu H, Huang J, Zhang X, Liu H, Cheng J and Tang C 2021 *Nuclear Fusion* **61** 036021
- [8] Varela J, Shimizu A, Spong D, Garcia L and Ghai Y 2021 *Nuclear Fusion* **61** 026023
- [9] Heidbrink W and Sadler G 1994 *Nuclear Fusion* **34** 535–615
- [10] Chen L 1994 *Physics of Plasmas* **1** 1519
- [11] Briguglio S Z F and G V 1998 *Physics of Plasmas* **5** 3287
- [12] Heidbrink W W 2008 *Physics of Plasmas* **15** 055501
- [13] Todo Y 2006 *Physics of Plasmas* **13** 082503
- [14] Todo Y, Berk H and Breizman B 2010 *Nuclear Fusion* **50** 084016

## REFERENCES

22

- [15] Todo Y, Seki R, Spong D A, Wang H, Suzuki Y, Yamamoto S, Nakajima N and Osakabe M 2017 *Physics of Plasmas* **24** 081203 ISSN 1089-7674
- [16] Park W, Parker S, Biglari H, Chance M, Chen L, Cheng C Z and Hahn T S 1992 *Physics Fluids B* **4** 2033
- [17] Bierwage A, Todo Y, A N and K S 2016 *Nuclear Fusion* **56** 106009
- [18] Sato M and Todo Y 2020 *Journal of Plasma Physics* **86** 815860305
- [19] Wang H, Todo Y, Osakabe M, Ido T and Suzuki Y 2019 *Nuclear Fusion* **59** 096041
- [20] Hirshman S P and Whitson J C 1983 *The Physics of Fluids* **26** 3553–3568
- [21] Suzuki Y, Nakajima N, Watanabe K, Nakamura Y and Hayashi T 2006 *Nuclear Fusion* **46** L19
- [22] Wang H, Todo Y, Ido T and Suzuki Y 2018 *Phys. Rev. Lett.* **120**(17) 175001
- [23] Wang H, Todo Y, Osakabe M, Ido T and Suzuki Y 2020 *Nuclear Fusion* **60** 112007
- [24] Spong D A, Sanchez R and Weller A 2003 *Physics of Plasmas* **10** 3217–3224
- [25] Li Y M and Ross D 1987 *Physics of Fluids* **30** 1466
- [26] Kerner W, Borba D, Huysmans G T A, Porcelli F, Poedts S, Goedbloed J P and Betti R 1994 *Plasma Physics and Controlled Fusion* **36** 911
- [27] Spong D A 2021 Stellgap <https://github.com/ORNL-Fusion/Stellgap>
- [28] Todo Y 2019 *Reviews of Modern Plasma Physics* **3** 1
- [29] Kolesnichenko Y I, Lutsenko V V, Wobig H and Yakovenko V 2002 *Physics of Plasmas* **9** 517
- [30] Kolesnichenko Y I, Lutsenko V V, Weller A, Werner A, Yakovenko Y V, Geiger J and Fesenyuk O P 2007 *Physics of Plasmas* **14** 102504